

BCS superconductivity near the band edge: exact results for one and several bands

D. Valentinis, D. van der Marel, and C. Berthod*

Department of Quantum Matter Physics (DQMP), University of Geneva,
24 quai Ernest-Ansermet, 1211 Geneva 4, Switzerland

(Dated: January 19, 2016)

We revisit the problem of a BCS superconductor in the regime where the Fermi energy is smaller than the Debye energy. This regime is relevant for low-density superconductors such as SrTiO₃ that are not in the BEC limit, as well as in the problem of “shape resonances” associated with the confinement of a three-dimensional superconductor. While the problem is not new, exact results were lacking in the low-density limit. In two dimensions, we find that the initial rise of the critical temperature T_c at low density n is nonanalytic and faster than any power of n . In three dimensions, we also find that T_c is nonanalytic, but starts with *zero* slope at weak coupling and infinite slope at strong coupling. Self-consistent treatment of the chemical potential and energy dependence of the density of states are crucial ingredients to obtain these results. We also present exact results for multi-band systems and confirm our analytical expressions by numerical simulations.

PACS numbers: 74.20.Fg, 74.62.Yb, 74.70.Ad

I. INTRODUCTION

The Bardeen–Cooper–Schrieffer (BCS) theory¹ remains the only strong microscopic foundation to support our understanding of the fascinating phenomenon of superconductivity. Among many other insights, the theory provides a simple expression for the critical temperature T_c , which continues to inspire the search for materials with improved performances. In particular, it is expected that superconductivity is favored by a low dimensionality due to enhanced density of states (DOS) at the Fermi level.² For three-dimensional (3D) materials, an early proposal to use quantum confinement in a thin film³ has received sustained attention until recently.⁴ The confinement-induced two-dimensional (2D) subbands produce discontinuities in the DOS and abrupt changes of T_c as a function of film thickness have been routinely predicted (so-called shape resonances).

The purpose of this study is to explore some consequences of an aspect of the problem, considered by Eagles half a century ago,^{2,5} but often overlooked in recent calculations based on the BCS gap equation. As the Fermi energy crosses the edge of a band, there is a regime where the dynamical cutoff of the pairing interaction is controlled by the band edge (Fig. 1). This regime is realized in low-density electron gases, when the Fermi energy is smaller than the dynamical range of the interaction. In doped SrTiO₃ for instance, the carrier concentration is typically 10^{19} cm^{-3} and the carrier mass is in the range 2–4 electronic masses,⁶ corresponding to a Fermi temperature of 50–100 K, while the Debye temperature is 513 K.⁷ In this situation, the common approximation of taking a constant DOS over the full dynamical range fails to give a good estimate for T_c . The near-band edge regime is also relevant in the quasi-2D problem of shape resonances, since each resonance is due to the Fermi energy crossing a subband edge. The pairing in that subband, as well as the inter-subband pairing involving that subband, are dominated by the band edge. A synthesis of these two cases is realized in the quasi-2D and low-density electron gas at the LaAlO₃/SrTiO₃ interface.^{8–10}

In the present paper, we focus on the band-edge effect on T_c in the bulk, emphasizing the generic behaviors in the simple case of an electron gas with parabolic dispersion and a local attraction. We recover the expressions of Eagles² in the weak-coupling limit. In the low-density regime, we provide exact relations as a function of the density, which are valid at arbitrary coupling. We also give exact numerical results in 2D and 3D, for one-band and multi-band systems. The implications for the problem of quasi-2D shape resonances and the case of LaAlO₃/SrTiO₃, will be reported in separate publications.

Our starting point is the gap equation for a momentum-independent pairing interaction acting in a limited energy range around the Fermi surface. We shall not be concerned with upstream assumptions leading to this equation, but refrain from making any further downstream approximation when solving it for the mean-field T_c . We leave aside the question whether realistic systems will show a superconducting transition at this temperature, or rather precursors of pairing.^{11,12} In particular, we ignore a possible breakdown

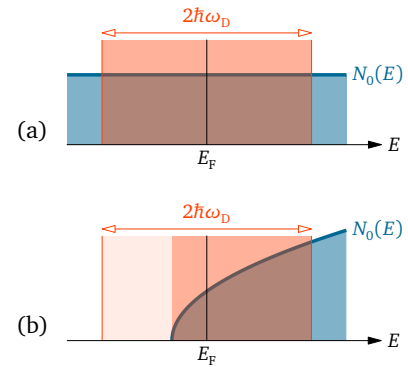


FIG. 1. Schematic representation of (a) the high-density regime and (b) the low-density regime for superconducting pairing. In the former, $E_F \gg \hbar\omega_D$ and the density of states $N_0(E)$ can be taken constant. In the latter, $E_F \lesssim \hbar\omega_D$, the interaction is cut by the band edge, and the details of $N_0(E)$ matter.

of this equation in the limit of vanishing density, associated with the formation and Bose-Einstein condensation of molecular pairs.^{13,14} In this respect, we stress that the band-edge effect discussed here is different from that considered in Ref. 15.

An exact solution of the gap equation requires to take into account the energy dependence of the DOS, most importantly the cutoff at the band bottom, and the temperature dependence of the chemical potential μ , which is crucial at low-density n . Because n , T_c , and μ all approach zero simultaneously, it is essential to use the exact relation $\mu(n, T_c)$ in order to capture the correct behavior of T_c for $n \rightarrow 0$. Furthermore, one should not assume weak coupling and/or assume that the critical temperature is small with respect to the Fermi energy and the cutoff for pairing. As a matter of fact, analytical results in this problem are rare. In Ref. 16, rigorous bounds for T_c were obtained for a general interaction. These results are limited to weak coupling and to a positive chemical potential. We will see that the chemical potential at T_c is in fact negative in the low-density limit in 2D for any coupling and in 3D for couplings larger than a critical value. Exact results have also been reported for the zero-temperature gap in 2D.¹⁷ However, since the universal BCS gap to T_c ratio is *not* obeyed in the low-density limit, these results cannot be used to deduce T_c .

This paper is the first in a series and it provides the mathematical foundations for subsequent studies dedicated to shape resonances in thin films and to the LaAlO₃/SrTiO₃ interface. It is organized as follows. In Sec. II we recall the basic coupled equations giving n and T_c and we write them in a dimensionless form, for one and several parabolic bands. In Sec. III we present our analytical and numerical results for one band in 2D and 3D, and in Sec. IV we briefly discuss multi-band effects.

II. BCS T_c EQUATION FOR MULTI-BAND SYSTEMS

A. Dimensionless equations for the critical temperature

We consider a multi-band metal with a local BCS pairing interaction $-V_{\alpha\beta}$ acting between electrons of opposite momenta and spins in bands α and β . We assume that Cooper pairing occurs only for two electrons in the same band, leading below the critical temperature T_c to an order parameter Δ_α in each band. This includes the possibility of a “proximity” induced gap Δ_β in a band that otherwise feels no pairing potential ($V_{\beta\beta} = 0$), via the nonzero inter-band interactions $V_{\alpha\beta}$. The BCS gap equation for Δ_α is

$$\Delta_\alpha = \sum_\beta V_{\alpha\beta} \Delta_\beta \int_{-\hbar\omega_D}^{\hbar\omega_D} d\xi N_{0\beta}(\mu + \xi) \frac{\tanh\left(\frac{\sqrt{\xi^2 + \Delta_\beta^2}}{2k_B T}\right)}{2\sqrt{\xi^2 + \Delta_\beta^2}}. \quad (1a)$$

The pairing interaction acts in a range $\pm\hbar\omega_D$ around the chemical potential μ . Although the notation $\hbar\omega_D$ is used here, our results are not restricted to phonon-mediated pairing, but apply to any local interaction with a dynamical

cutoff. $N_{0\beta}(E)$ is the DOS per spin and per unit volume for the band β . It is defined on an absolute energy scale, such that $N_{0\beta}(\mu)$ is the DOS at the chemical potential μ , which is common to all bands. The chemical potential must be adjusted to fix the density according to

$$n = 2 \int_{-\infty}^{\infty} dE f(E) N(E). \quad (1b)$$

Here, $f(E) = [e^{(E-\mu)/k_B T} + 1]^{-1}$ is the Fermi distribution function and $N(E)$ is the total BCS density of states (per spin) resulting from the opening of the superconducting gaps at the chemical potential in each band.

For the calculation of T_c , it is sufficient to consider the two equations in the limit of vanishing order parameters. We assume that all gaps approach zero at the same T_c , with the ratios $\Delta_\beta/\Delta_\alpha$ fixed by the gap equation (1a). For $T = T_c$, we have

$$1 = \sum_\beta V_{\alpha\beta} \frac{\Delta_\beta}{\Delta_\alpha} \int_{-\hbar\omega_D}^{\hbar\omega_D} dE N_{0\beta}(\mu + E) \frac{\tanh\left(\frac{E}{2k_B T_c}\right)}{2E} \quad (2a)$$

$$n = 2 \int_{-\infty}^{\infty} dE f(E) \sum_\beta N_{0\beta}(E). \quad (2b)$$

We now insert explicit formulas for the densities of states and the density and we rewrite the equations (2) in a dimensionless form, which is more convenient for analytical and numerical treatments. The densities of states for a parabolic band in dimensions $d = 2$ and $d = 3$ are given by

$$N_{0\beta}(E) = (d-1)\pi \left(\frac{m_\beta}{2\pi^2\hbar^2}\right)^{\frac{d}{2}} \theta(E - E_{0\beta}) (E - E_{0\beta})^{\frac{d}{2}-1}, \quad (3)$$

where m_β is the band mass, $E_{0\beta}$ is the energy of the band minimum and θ is the Heaviside function. This definition ensures that $N_{0\beta}(\mu)$ is the DOS evaluated at the chemical potential μ common to all bands, consistently with Eq. (1a). The relation between density, chemical potential and temperature for a parabolic band in arbitrary dimension d is

$$n = -2 \left(\frac{mk_B T}{2\pi\hbar^2}\right)^{\frac{d}{2}} \text{Li}_{\frac{d}{2}}\left(-e^{\frac{\mu-E_0}{k_B T}}\right), \quad (4)$$

where $\text{Li}_p(x)$ is the polylogarithm given by the series expansion $\text{Li}_p(x) = \sum_{q=1}^{\infty} x^q/q^p$. This function has the sign of its argument and reduces to a usual logarithm in two dimensions ($p = 1$): $\text{Li}_1(x) = -\ln(1-x)$. We provide a brief derivation of Eq. (4) in Appendix A for the interested reader.

We measure all energies in units of $\hbar\omega_D$, express the density in units of $2[m\omega_D/(2\pi\hbar)]^{d/2}$ where m is a reference mass, and we distinguish the dimensionless variables with tildes, e.g.

$$\tilde{T}_c = \frac{k_B T_c}{\hbar\omega_D}, \quad \tilde{\mu} = \frac{\mu}{\hbar\omega_D}, \quad \tilde{n} = \frac{n}{2[m\omega_D/(2\pi\hbar)]^{d/2}}, \quad \text{etc.}$$

The coupled equations (2) for T_c become

$$1 = \sum_{\beta} \bar{\lambda}_{\alpha\beta} \psi_d \left(1 + \tilde{\mu} - \tilde{E}_{0\beta}, \tilde{T}_c \right) \Delta_{\beta} / \Delta_{\alpha} \quad (5a)$$

$$\tilde{n} = -\tilde{T}_c^{\frac{d}{2}} \sum_{\beta} \left(\frac{m_{\beta}}{m} \right)^{\frac{d}{2}} \text{Li}_{\frac{d}{2}} \left(-e^{\frac{\tilde{\mu} - \tilde{E}_{0\beta}}{\tilde{T}_c}} \right). \quad (5b)$$

We have introduced the dimensionless function

$$\psi_d(a, b) = \theta(a) \int_{1-\min(a,2)}^1 dx (x+a-1)^{\frac{d}{2}-1} \frac{\tanh\left(\frac{x}{2b}\right)}{2x}, \quad (6)$$

as well as the coupling constants

$$\bar{\lambda}_{\alpha\beta} = V_{\alpha\beta}(d-1)\pi \left(\frac{m_{\beta}}{2\pi^2\hbar^2} \right)^{\frac{d}{2}} (\hbar\omega_D)^{\frac{d}{2}-1}. \quad (7)$$

We use a bar to recall that these coupling constants are not evaluated at the Fermi energy like in the common practice, but at an energy $\hbar\omega_D$ above the bottom of each band, $\bar{\lambda}_{\alpha\beta} = V_{\alpha\beta}N_{0\beta}(E_{0\beta} + \hbar\omega_D)$. This choice is natural and leads to the simplest equations. The usual definition $\lambda = VN_0(\mu)$ poses problem when μ lies below the band bottom and more generally because μ is a function of interaction strength and temperature.

In a N band system, the relations (5) provide $N+1$ equations for the $N+1$ unknowns, which are \tilde{T}_c , $\tilde{\mu}$, and the $N-1$ ratios Δ_{β}/Δ_1 . We now eliminate the $N-1$ gap ratios and reduce the problem to a pair of equations for \tilde{T}_c and $\tilde{\mu}$. With the new definitions $r_{\beta} = \Delta_{\beta}/\Delta_1$ and

$$\Lambda_{\alpha\beta}(\tilde{\mu}, \tilde{T}_c) = \bar{\lambda}_{\alpha\beta} \psi_d(1 + \tilde{\mu} - \tilde{E}_{0\beta}, \tilde{T}_c), \quad (8)$$

the set of N equations (5a) becomes the eigenvalue problem $\Lambda \mathbf{r} = \mathbf{r}$ with $\mathbf{r} = (1, r_2, \dots, r_N)$. This means that, when evaluated at a value of \tilde{T}_c solving Eq. (5a), the matrix Λ has at least one unit eigenvalue. In other words, \tilde{T}_c corresponds to the largest temperature that satisfies the characteristic equation $\det(\mathbb{1} - \Lambda) = 0$. The two coupled dimensionless equations giving n and T_c for N bands are therefore

$$0 = \det[\mathbb{1} - \Lambda(\tilde{\mu}, \tilde{T}_c)] \quad (9a)$$

$$\tilde{n} = -\tilde{T}_c^{\frac{d}{2}} \sum_{\alpha=1}^N \left(\frac{m_{\alpha}}{m} \right)^{\frac{d}{2}} \text{Li}_{\frac{d}{2}} \left(-e^{\frac{\tilde{\mu} - \tilde{E}_{0\alpha}}{\tilde{T}_c}} \right). \quad (9b)$$

The equations (9) have the same structure in 2D and 3D, the quantitative differences stemming mostly from different functions $\psi_d(a, b)$. In the next paragraph, we discuss the properties of these functions, which we shall use in the next sections to derive analytical results.

B. Properties of the functions $\psi_d(a, b)$

The functions $\psi_d(a, b)$ are displayed¹⁸ in Fig. 2. The strongest structure develops around $a = 1$, which correspond physically to having the chemical potential at the

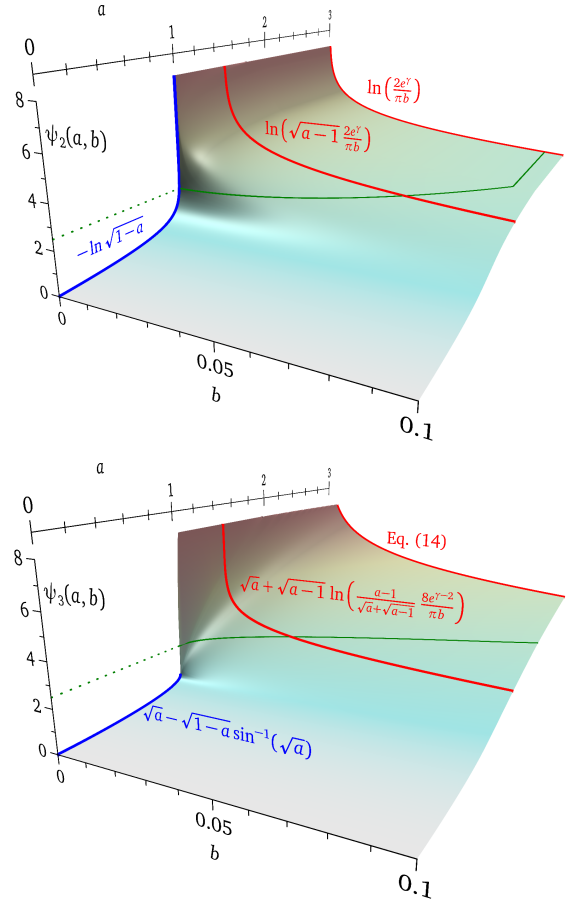


FIG. 2. Representation of the functions $\psi_d(a, b)$ defined in Eq. (6) for dimensions $d = 2$ (top) and $d = 3$ (bottom). Physically, the a axis corresponds to varying μ around the band bottom ($a = 1$) and the b axis is proportional to T_c . The blue lines show the behavior for $b = 0$ and $a < 1$. The two red lines in each graph show the asymptotic b -dependencies for $1 < a < 2$ and $a > 2$, respectively. The green lines show cuts at the value $\psi_d(a, b) = 2.5$, which correspond to the path followed in the (a, b) plane by the solution of the BCS equations (9) for one band and for $\bar{\lambda} = 0.4$.

bottom of one band. We are mostly interested in the behavior for $b \ll 1$, which is explored in the regime $k_B T_c \ll \hbar\omega_D$ and particularly in the limit $b \rightarrow 0$, which is relevant when the density approaches zero. If $a < 1$, $\psi_d(a, b)$ is finite for $b = 0$. The limiting value is given by

$$\begin{aligned} \psi_d(0 < a < 1, b \rightarrow 0) &= \int_{\frac{1-a}{b}}^{\frac{1}{b}} dx \frac{(bx+a-1)^{\frac{d}{2}-1}}{2x} \\ &= \begin{cases} -\ln \sqrt{1-a} & (d=2) \\ \sqrt{a-\sqrt{1-a}} \sin^{-1}(\sqrt{a}) & (d=3). \end{cases} \end{aligned} \quad (10)$$

These limiting behaviors are indicated on the graphs as blue lines. If $a > 1$, $\psi_d(a, b)$ diverges logarithmically for $b \rightarrow 0$, but in different ways in the two ranges $1 < a < 2$ and $a > 2$. The former range corresponds physically to

$0 < \mu < \hbar\omega_D$, such that the band edge sets the lower cutoff for the pairing interaction, while the latter range is the usual regime, where the Fermi energy is larger than the Debye energy. In two dimensions, the asymptotic behavior is quite simple: if $a > 2$, we have the well-known result

$$\psi_2(a > 2, b \rightarrow 0) = \int_{-\frac{1}{b}}^{\frac{1}{b}} dx \frac{\tanh(x/2)}{2x} = \ln\left(\frac{2e^\gamma}{\pi b}\right), \quad (11)$$

with $\gamma \approx 0.577$ the Euler constant. The function is independent of a , because the DOS is constant over the range of integration when $\mu > \hbar\omega_D$. If $1 < a < 2$, we evaluate the function by extending the integral to reproduce the case $a > 2$ and subtracting the difference:

$$\begin{aligned} \psi_2(1 < a < 2, b \rightarrow 0) &= \int_{-\frac{1}{b}}^{\frac{1}{b}} dx \frac{\tanh(x/2)}{2x} - \int_{-\frac{1}{b}}^{\frac{1-a}{b}} dx \frac{-1}{2x} \\ &= \ln\left(\sqrt{a-1} \frac{2e^\gamma}{\pi b}\right). \end{aligned} \quad (12)$$

Equations (11) and (12) are represented in Fig. 2(top) as red lines. In order to obtain the exact asymptotic behavior for $b \rightarrow 0$ in three dimensions, we introduce the function $t(x)$ as a piece-wise linear approximation of $\tanh(x/2)$ —namely, -1 for $x < -2$, $x/2$ for $|x| < 2$, and $+1$ for $x > 2$ —and we calculate analytically the integral with $\tanh(x/2)$ replaced by $t(x)$. The difference between the latter approximation and the exact result is

$$\begin{aligned} \lim_{b \rightarrow 0} \int_{\frac{1-\min(a,2)}{b}}^{\frac{1}{b}} dx \sqrt{bx+a-1} \frac{\tanh(x/2) - t(x)}{2x} \\ = \sqrt{a-1} \ln\left(\frac{4e^{\gamma-1}}{\pi}\right). \end{aligned}$$

Expanding the nonsingular terms to leading order in b , we finally get in the regime $0 < \mu < \hbar\omega_D$:

$$\begin{aligned} \psi_3(1 < a < 2, b \rightarrow 0) \\ = \sqrt{a} + \sqrt{a-1} \ln\left(\frac{a-1}{\sqrt{a} + \sqrt{a-1}} \frac{8e^{\gamma-2}}{\pi b}\right), \end{aligned} \quad (13)$$

and in the regime $\mu > \hbar\omega_D$:

$$\begin{aligned} \psi_3(a > 2, b \rightarrow 0) &= \sqrt{a} + \sqrt{a-2} + \sqrt{a-1} \\ &\times \ln\left(\frac{a-1}{\sqrt{a} + \sqrt{a-1}} \sqrt{\frac{\sqrt{a-1} - \sqrt{a-2}}{\sqrt{a-1} + \sqrt{a-2}}} \frac{8e^{\gamma-2}}{\pi b}\right). \end{aligned} \quad (14)$$

These asymptotic behaviors are indicated in Fig. 2(bottom) as red lines. Lastly, in the high-density, high- T_c sector $a > 2$ and $b \rightarrow \infty$, the function reduces simply to $\psi_d(a, b) = (a-1)^{d/2-1}/(2b)$.

Figure 2 also shows a particular cut at the value $\psi_d = 2.5$. Since the BCS equation (9a) for one band is simply $\psi_d =$

$1/\bar{\lambda}$, these cuts show the locus of the solutions $(a, b) = (1 + \tilde{\mu}, \tilde{T}_c)$ for $\bar{\lambda} = 0.4$. Note that the approximations (11) to (14) shown in red underestimate the function ψ_d at low b ; using them instead of the exact functions thus leads to underestimating T_c .

III. ONE PARABOLIC BAND IN 2D AND 3D

A. Analytical results

For a single band, we place the origin of energy at the bottom of the band and we use the band mass as the reference mass. The coupled equations (9) for T_c become simply:

$$1 = \bar{\lambda} \psi_d(1 + \tilde{\mu}, \tilde{T}_c), \quad \tilde{n} = -\tilde{T}_c^{\frac{d}{2}} \text{Li}_{\frac{d}{2}}(-e^{\tilde{\mu}/\tilde{T}_c}). \quad (15)$$

These two equations must be solved self-consistently for the chemical potential and the critical temperature, at each value of the density. In 2D, the relation between \tilde{n} and $\tilde{\mu}$ can be trivially inverted and the two equations reduce to a single implicit relation for \tilde{T}_c as a function of \tilde{n} and $\bar{\lambda}$:

$$1 = \bar{\lambda} \psi_2\left(1 + \tilde{T}_c \ln(e^{\tilde{n}/\tilde{T}_c} - 1), \tilde{T}_c\right). \quad (16)$$

At not too low density, when μ is of order $\hbar\omega_D$, we see from the asymptotic expressions indicated in Fig. 2 that the critical temperature crosses over between two different behaviors at $\tilde{\mu} = 1$. In 2D we have

$$\tilde{T}_c \approx \frac{2e^\gamma}{\pi} \exp\left(-\frac{1}{\bar{\lambda}}\right) \times \begin{cases} \sqrt{\tilde{\mu}} & \tilde{\mu} \lesssim 1 \\ 1 & \tilde{\mu} > 1 \end{cases} \quad (d=2). \quad (17)$$

\tilde{T}_c is independent of $\tilde{\mu}$ (hence of \tilde{n}) for $\tilde{\mu} > 1$, due to the constant DOS and the conventional BCS expression is recovered. In 3D we find

$$\begin{aligned} \tilde{T}_c \approx \frac{8e^{\gamma-2}}{\pi} \sqrt{\tilde{\mu}} \exp\left(-\frac{1}{\bar{\lambda}\sqrt{\tilde{\mu}}}\right) \frac{e^{\sqrt{1+1/\tilde{\mu}}}}{1 + \sqrt{1+1/\tilde{\mu}}} \\ \times \begin{cases} 1 & \tilde{\mu} \lesssim 1 \\ e^{\sqrt{1-1/\tilde{\mu}}} \sqrt{\frac{1-\sqrt{1-1/\tilde{\mu}}}{1+\sqrt{1-1/\tilde{\mu}}}} & \tilde{\mu} > 1 \end{cases} \quad (d=3). \end{aligned} \quad (18)$$

Since $\bar{\lambda}$ is evaluated at an energy $\hbar\omega_D$ above the bottom of the band, the product $\bar{\lambda}\sqrt{\tilde{\mu}}$ is the coupling constant evaluated at the chemical potential, which appears in the exponential as expected. Equations (17) and (18) are the same as Eqs. (2) and (3) of Ref. 2, despite a slightly different writing, if we admit that $k_B T_c = (e^\gamma/\pi)\Delta$, which is true in the regime of validity of these expressions—but not in the low-density and/or strong-coupling regimes, see below. We emphasize that these approximations result from expanding the function $\psi_d(a, b)$ in the limit $b \rightarrow 0$ for $a > 1$ and are

therefore accurate only in the limit $T_c \rightarrow 0$ at finite positive μ . These conditions are fulfilled in the weak-coupling regime $\bar{\lambda} \rightarrow 0$, at not too low density. These equations are not accurate in the high-density regime where T_c is large and keeps growing with increasing n in 3D. Our numerical results show that, as soon as T_c reaches a few tenths of $\hbar\omega_D$, Eqs. (17–18) provide a rather poor approximation.

We now turn to the low-density region, where the behaviors are qualitatively different in 2D and 3D. In 2D any cut of the function $\psi_2(a, b)$ at the value $1/\bar{\lambda}$ converges at $b = 0$ to a value $a < 1$, given by the relation $-\ln \sqrt{1-a} = 1/\bar{\lambda}$ (see Fig. 2). Hence the chemical potential converges to a finite negative value $\tilde{\mu}_{\min} = -e^{-2/\bar{\lambda}}$ when the density approaches zero. This is a conjugated effect of the pairing interaction and the DOS discontinuity: at any finite coupling, the momentum distribution is spread and a negative chemical potential leads to a finite density even at zero temperature. Note that we are dealing here with the chemical potential at T_c , such that a negative value does not necessarily mean that one has entered the BEC regime. Equation (16) for $\tilde{T}_c \rightarrow 0$ becomes $1 = -\bar{\lambda} \ln \sqrt{-\tilde{T}_c \ln(e^{\tilde{n}/\tilde{T}_c} - 1)}$, which can be solved for \tilde{n} as a function of \tilde{T}_c : $\tilde{n} = \tilde{T}_c \ln\{1 + \exp[-\exp(-2/\bar{\lambda})/\tilde{T}_c]\}$. The latter expression cannot be inverted analytically to yield \tilde{T}_c as a function of \tilde{n} . However it shows that \tilde{n} is smaller than \tilde{T}_c when both approach zero, such that in this limit we can replace $\ln(e^{\tilde{n}/\tilde{T}_c} - 1)$ by $\ln(\tilde{n}/\tilde{T}_c)$. We thus find the solution

$$\tilde{T}_c = \tilde{n} \exp \left[W \left(\frac{e^{-2/\bar{\lambda}}}{\tilde{n}} \right) \right] \quad (d = 2, n \rightarrow 0). \quad (19)$$

$W(x)$ is the Lambert function (or “product logarithm”), which gives the principal solution of the equation $x = We^x$. Equation (19) is nonanalytic in both $\bar{\lambda}$ and \tilde{n} . It gives a critical temperature starting with an infinite slope at $n = 0$ and increasing faster than any power of n (in the sense that the running exponent given by the logarithmic derivative approaches zero for $n \rightarrow 0$).

In 3D the function $\psi_3(a < 1, 0)$ approaches 1 (with infinite slope) for $a \rightarrow 1$ [Eq. (10)]. Therefore we have the same situation as in 2D if $\bar{\lambda} > 1$. In this case the chemical potential approaches a finite negative value given by the solution of $\sqrt{\tilde{\mu}_{\min} + 1} - \sqrt{-\tilde{\mu}_{\min}} \sin^{-1}(\sqrt{\tilde{\mu}_{\min} + 1}) = 1/\bar{\lambda}$ as the density approaches zero. Here, unlike in 2D, the DOS vanishes continuously at the band bottom: this may explain why a finite coupling $\bar{\lambda} > 1$ is necessary to generate a finite density when the chemical potential is negative. Since $\tilde{\mu}$ is finite and negative in the limit $\tilde{T}_c \rightarrow 0$, we can use the asymptotic expression of $-\text{Li}_{3/2}(-e^x)$ for $x \rightarrow -\infty$ in Eq. (15), which is e^x , and get the chemical potential as $\tilde{\mu} = \tilde{T}_c \ln(\tilde{n}/\tilde{T}_c^{3/2})$. Equation (15) can then be solved for \tilde{T}_c in the relevant regime $-\tilde{\mu} \ll 1$, by making use of Eq. (10) to leading order in $1 - a$. This yields

$$\tilde{T}_c \approx \tilde{n}^{2/3} \exp \left[W \left(\frac{8(1/\bar{\lambda} - 1)^2}{3\pi^2 \tilde{n}^{2/3}} \right) \right] \quad (d = 3, \bar{\lambda} > 1, n \rightarrow 0). \quad (20)$$

Like in 2D, T_c starts in 3D with an infinite slope at $n = 0$ if $\bar{\lambda} > 1$ and increases faster than any power of n . If $\bar{\lambda} < 1$, however, there is no finite solution a to the equation $\psi_3(a, 0) = 1/\bar{\lambda}$, meaning that μ goes to zero at zero density. As can be seen in Fig. 2(bottom), the curvature along the cut for $\psi_3 > 1$ is such that $\tilde{\mu} > \tilde{T}_c$. In the limit $\tilde{T}_c \rightarrow 0$, we can therefore use the large- x expansion of $-\text{Li}_{3/2}(-e^x)$, namely $4/(3\sqrt{\pi})x^{3/2}$, and recover $\tilde{\mu} = (3\sqrt{\pi}\tilde{n}/4)^{2/3}$, which is the zero-temperature noninteracting result. Using the asymptotic form (13) for ψ_3 , we finally obtain

$$\tilde{T}_c = \frac{8e^{\gamma-2}}{\pi} \left(\frac{3\sqrt{\pi}\tilde{n}}{4} \right)^{2/3} \exp \left[- \left(\frac{1}{\bar{\lambda}} - 1 \right) \left(\frac{4}{3\sqrt{\pi}\tilde{n}} \right)^{1/3} \right] \quad (d = 3, \bar{\lambda} < 1, n \rightarrow 0). \quad (21)$$

This function starts with zero slope at $n = 0$ and increases slower than any power of n . Note that, according to Eqs. (20) and (21), the change of behavior at $\bar{\lambda} = 1$ is discontinuous, since both functions give $\tilde{T}_c \propto \tilde{n}^{2/3}$ for $\bar{\lambda} = 1$, but with different pre-factors.

The analytical expressions (17–21) are compared below with the numerical results. Note that the band mass, which does not appear explicitly in these analytical formula, is actually hidden in the normalization of n . If the reference mass m is not the band mass m_a , one must replace \tilde{n} by $\tilde{n}(m/m_a)^{d/2}$ in Eqs. (17–21).

We have not discussed the band-edge effect in one dimension (1D), because the BCS mean-field theory is not believed to be a useful model in 1D. Nevertheless, it has been argued that the square-root singularity of the 1D DOS could induce large enhancements of T_c in striped quasi-1D superconductors.²⁰ For completeness, we show in Appendix B that the BCS critical temperature is continuous and nonanalytic at the bottom of a 1D band, like in 2D and 3D, although the nonanalyticity is stronger as expected.

Before closing this section, we point out that the solution of the gap equation at $T = 0$, which may appear simpler to obtain, does not generally allow to deduce T_c . Although the focus of the present paper is on T_c , we give exact results in Appendix C for the zero-temperature gap in 2D at low density, for the purpose of showing that the usual BCS gap to T_c ratio is not obeyed in this limit.

B. Numerical results

The numerical solution of Eq. (16) is shown in Fig. 3. \tilde{T}_c reaches a plateau at high density due to the constant DOS of the band. For $\bar{\lambda}$ of order one, the value $T_{c,\infty}$ on the plateau departs significantly from the approximate solution (17), which underestimates \tilde{T}_c as indicated above. This approximation becomes worse with increasing $\bar{\lambda}$, while the simple result $\tilde{T}_{c,\infty} = \bar{\lambda}/2$, deduced from the asymptotics of $\psi_2(a, b)$ for large b , becomes increasingly reliable [inset of Fig. 3(b)]. The density \tilde{n}_∞ at which the plateau is reached corresponds to $\mu - \hbar\omega_D$ coinciding with the bottom of the

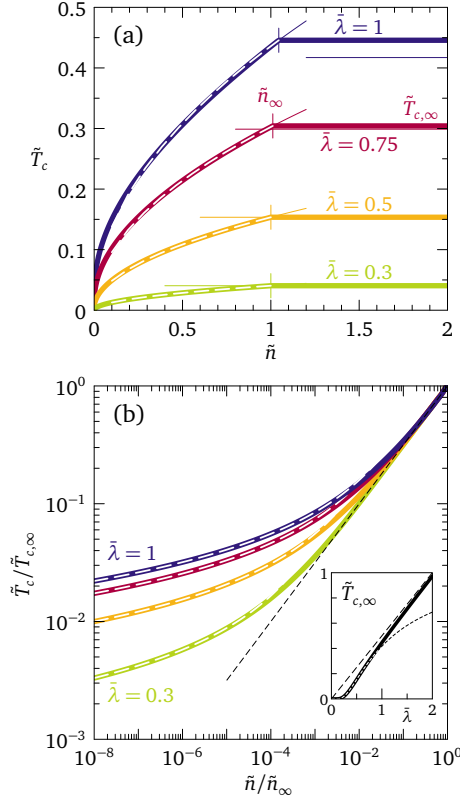


FIG. 3. (a) BCS critical temperature as a function of electron density for one parabolic band in two dimensions. T_c is expressed in units of $\hbar\omega_D/k_B$ and n in units of $m\omega_D/(\pi\hbar)$. The thin horizontal lines show the approximate solution (17) for each $\bar{\lambda}$. The vertical bars indicate \tilde{n}_∞ [Eq. (22)], where \tilde{T}_c reaches the value $\tilde{T}_{c,\infty}$. The dashed lines show that the approximate behavior $\tilde{T}_c = \tilde{T}_{c,\infty}(\tilde{n}/\tilde{n}_\infty)^{1/2}$ is well obeyed for $\tilde{n} \lesssim \tilde{n}_\infty$. (b) Same data normalized for $\tilde{n} < \tilde{n}_\infty$, showing the nonuniversal behavior at low density. The white dashed lines are the prediction of Eq. (19) and the black dashed line indicates the square-root behavior for $\tilde{n} \lesssim \tilde{n}_\infty$. (Inset) Maximum critical temperature as a function of $\bar{\lambda}$ (solid line), compared with Eq. (17) (dotted) and $\bar{\lambda}/2$ (dashed).

band, in other words $\tilde{\mu} = 1$ in our case, which means:

$$\tilde{n}_\infty = \tilde{T}_{c,\infty} \ln \left(e^{1/\tilde{T}_{c,\infty}} + 1 \right). \quad (22)$$

\tilde{n}_∞ approaches unity for small $\tilde{T}_{c,\infty}$. For $\tilde{n} \lesssim \tilde{n}_\infty$, Eq. (17) gives $\tilde{T}_c/\tilde{T}_{c,\infty} \approx \tilde{\mu}^{1/2}$. Since $\tilde{\mu}$ is very close to a linear function of \tilde{n} at intermediate and high densities (see below), we expect to have the universal scaling $\tilde{T}_c/\tilde{T}_{c,\infty} \approx (\tilde{n}/\tilde{n}_\infty)^{1/2}$. This is well obeyed by the data, as illustrated in Fig. 3.

Close to $\tilde{n} = 0$, however, the behavior is nonuniversal, in the sense that the curves do not collapse if \tilde{n} and \tilde{T}_c are rescaled by \tilde{n}_∞ and $\tilde{T}_{c,\infty}$, respectively [Fig. 3(b)]. The numerical data are in perfect agreement with the limiting behavior (19) at all couplings. The running exponent $\eta(n)$ in $T_c \propto n^{\eta(n)}$ approaches zero for $n \rightarrow 0$, as illustrated by the flattening of the curves in the log-log plot. This is suggestive of a discontinuity of $T_c(n)$ at $n = 0$, as if T_c would jump due to the discontinuity of the 2D DOS. However, since Eq. (19)

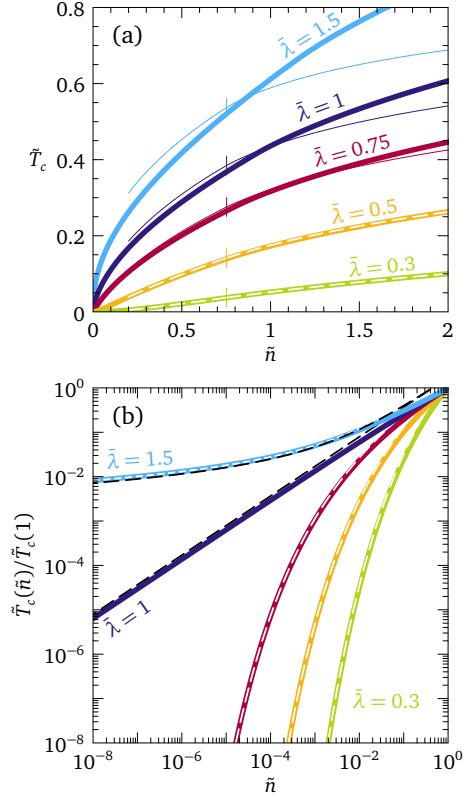


FIG. 4. (a) BCS critical temperature as a function of electron density for one parabolic band in three dimensions. T_c is expressed in units of $\hbar\omega_D/k_B$ and n in units of $2[m\omega_D/(2\pi\hbar)]^{3/2}$. The thin and dashed lines show Eq. (18), evaluated using $\tilde{\mu}_0 = (3\sqrt{\pi}\tilde{n}/4)^{2/3}$ for $\tilde{\mu}$. The vertical bars indicate $\tilde{\mu}_0 = 1$. (b) Same data on a log-log scale. The dashed lines show Eqs. (20) and (21). Eq. (21) was used for $\bar{\lambda} = 1$. The short-dashed white line for $\bar{\lambda} = 1.5$ is obtained without expanding Eq. (10) around $a = 1$ (see text).

vanishes continuously for $\tilde{n} \rightarrow 0$ at any finite coupling, the correct picture is that of a T_c tending asymptotically to a discontinuity of size zero with decreasing n .

The numerical results for the 3D case are displayed in Fig. 4. Also shown is the high-density approximation (18), evaluated with $\tilde{\mu}$ replaced by its zero-temperature noninteracting value $\tilde{\mu}_0 = (3\sqrt{\pi}\tilde{n}/4)^{2/3}$. This approximation falls on top of the numerical data for small $\bar{\lambda}$, but deviates significantly, as in 2D, for larger coupling. The good agreement at weak coupling is due to a fortunate cancellation of errors. Indeed, using the exact $\tilde{\mu}$ instead of $\tilde{\mu}_0$ in Eq. (18), the agreement generally worsens. This is because $\mu(T_c) < \mu_0$ and T_c is a monotonically increasing function of μ , such that the substitution of μ_0 for $\mu(T_c)$ always leads to overestimating T_c . This happens to compensate the underestimation of T_c due to the use of Eqs. (13) and (14), which underestimate ψ_3 .

At low density, the change of behavior from a convex increase for $\bar{\lambda} < 1$ to a concave increase for $\bar{\lambda} > 1$ is visible on the log-log plot in Fig. 4(b)—where a convex function has a slope larger than unity. The low-density, low-coupling limit (21) describes the numerical data perfectly. The low-density,

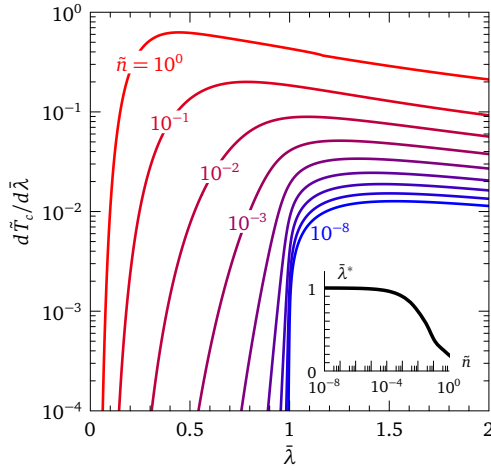


FIG. 5. Derivative of the critical temperature with respect to $\bar{\lambda}$ for one parabolic band in three dimensions. Each curve corresponds to a different density. (Inset) Crossover coupling $\bar{\lambda}^*$ defined by a maximum in $d^2\bar{T}_c/d\bar{\lambda}^2$, as a function of \bar{n} . T_c varies exponentially with coupling for $\bar{\lambda} < \bar{\lambda}^*$ and linearly for $\bar{\lambda} > \bar{\lambda}^*$.

high-coupling expression (20) shows the correct behavior, but deviates slightly from the numerical data, due to the use of Eq. (10) at lowest order in $1-a$. If we evaluate \bar{T}_c without expanding Eq. (10), this small discrepancy disappears. The value $\bar{\lambda} = 1$ is somewhat peculiar: the numerics shows the expected $\bar{n}^{2/3}$ scaling, but the pre-factor is neither unity as implied by Eq. (20), nor 0.742 as given by Eq. (21), but ~ 0.6 .

In Fig. 5 we plot $d\bar{T}_c/d\bar{\lambda}$ as a function of $\bar{\lambda}$. This representation highlights the dramatic change of behavior at $\bar{\lambda} = 1$. For $\bar{\lambda} > 1$, the derivative is large for any density and depends weakly on $\bar{\lambda}$: this is a regime where T_c increases more or less linearly with $\bar{\lambda}$. For $\bar{\lambda} < 1$, the derivative is small but increases steadily with $\bar{\lambda}$, such that in this range T_c varies exponentially with $\bar{\lambda}$. The crossover between the two regimes takes place at some value $\bar{\lambda}^*$, which is a decreasing function of increasing density. We find that the crossover appears most clearly as a maximum in the second derivative $d^2\bar{T}_c/d\bar{\lambda}^2$, which we use to define $\bar{\lambda}^*$. The dependency $\bar{\lambda}^*(\bar{n})$ is displayed in the inset.

Figure 6 (top row) shows the chemical potential at T_c in the low-density regime, calculated numerically for various $\bar{\lambda}$. In 2D μ converges to a negative value for any coupling, as discussed above. The range of densities where $\mu < 0$ sets the range of validity of Eq. (19), which shrinks as $\bar{\lambda}$ is reduced, as can be seen in Fig. 3(b). In 3D μ converges to a negative value at $n = 0$ if $\bar{\lambda} > 1$; if $\bar{\lambda} \leq 1$, it tends to zero. In both 2D and 3D one sees that the effect of increasing the pairing interaction is mainly to shift the $\mu(n)$ curve downwards. At $n = 0$ this shift is entirely due to the interaction-induced spreading of the momentum distribution. At finite n part of the shift is due to the thermal smearing, because μ is evaluated at T_c .

As the density increases, the behavior of the chemical potential is qualitatively different in 2D and 3D: while $\bar{\mu}$

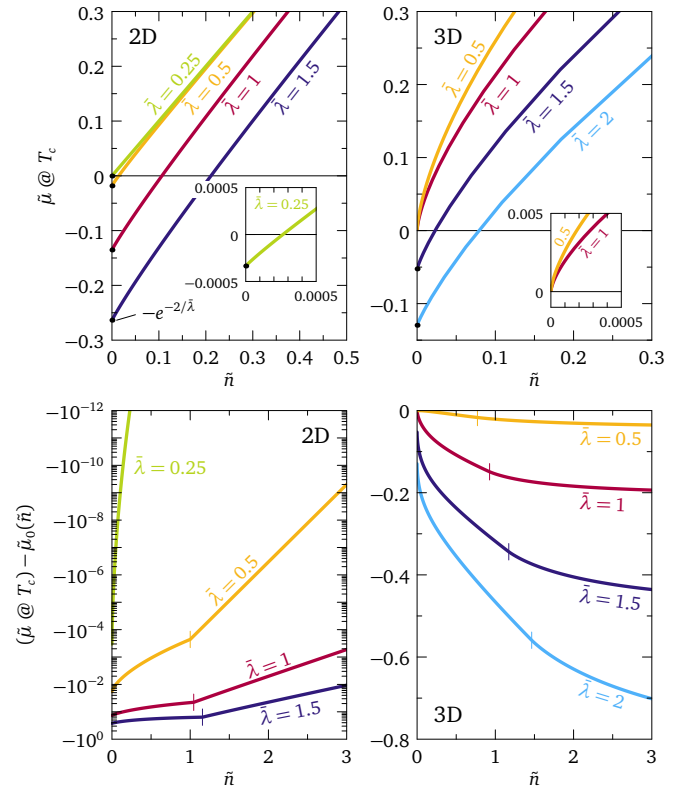


FIG. 6. Top row. Chemical potential at T_c in the low-density limit. The dots show the solution of $\psi_d(1 + \bar{\mu}, 0) = 1/\bar{\lambda}$, with $\psi_d(a, 0)$ given by Eq. (10). The insets show that $\mu(n=0) < 0$ in 2D for all $\bar{\lambda}$, while $\mu(n=0) = 0$ in 3D for $\bar{\lambda} \leq 1$. Bottom row. Difference between the chemical potential at T_c and the zero-temperature noninteracting value $\bar{\mu}_0 = \bar{n}$ in 2D and $\bar{\mu}_0 = (3\sqrt{\pi}\bar{n}/4)^{2/3}$ in 3D. Note the change of behavior at $\bar{\mu} = 1$, indicated by vertical bars.

approaches the zero-temperature noninteracting value $\bar{\mu}_0 = \bar{n}$ in 2D, this does not happen in 3D (Fig. 6, bottom row). In 2D the chemical potential at T_c is $\bar{\mu} = \bar{T}_c \ln(e^{\bar{n}/\bar{T}_c} - 1)$. Since \bar{T}_c saturates for $\bar{n} > \bar{n}_\infty$, we have $\bar{n} > \bar{T}_c$ at large \bar{n} and $\bar{\mu}$ approaches exponentially the value \bar{n} , for all coupling strengths. This is of course peculiar to the 2D constant DOS, since both interaction and temperature redistribute states in equal amounts below and above μ_0 . In 3D the square-root DOS implies that there are more states added in the tail of the momentum distribution above μ_0 , than there are states removed below μ_0 . The equilibrium chemical potential must therefore remain below the zero-temperature noninteracting value, by an amount which increases with increasing $\bar{\lambda}$ and also with increasing n , because T_c grows with increasing n .

IV. MULTI-BAND EFFECTS

The interest raised by multi-band superconductors, in particular MgB₂ and the iron-based family, has triggered many studies over the years.²¹ Here we discuss mostly multi-band effects that occur near a band edge and are associated with the low density in one of the bands.

It is clear from the previous section that a knowledge of the self-consistent chemical potential is required to understand the behavior of \tilde{T}_c close to a band minimum. This raises the question of the role played by perturbations that affect the chemical potential, such that the presence of a non-superconducting band (NB) beneath the superconducting band (SB). In the absence of inter-band coupling, the NB can only alter the superconducting properties of the SB by changing the chemical potential. In 2D and in 3D for $\tilde{\lambda} > 1$, the key observation was that μ is finite and negative at the band bottom, such that the nonanalytic behavior of T_c near the band edge is not controlled by μ . A NB is therefore not expected in general to change this nonanalytic behavior qualitatively. An exception—confirming the rule—occurs when the bottom of the NB coincides precisely with the energy at which the SB begins to be populated. For this peculiar arrangement, the NB controls the relation between μ and n in the limit $T_c \rightarrow 0$ and T_c displays a simple analytic dependence on n , which is linear in 2D and $\propto n^{2/3}$ in 3D. This is illustrated in Fig. 7(a) for the 2D case. We can understand it by solving the coupled equations (9) for two bands in the appropriate regime.

Consider two bands with masses m_1 and m_2 , minima $E_{01} \equiv 0$ and E_{02} , and coupling constants $\tilde{\lambda}_{11} > 0$ ($\tilde{\lambda}_{11} > 1$ in 3D) and $\tilde{\lambda}_{22} = \tilde{\lambda}_{12} = 0$. The initial rise of T_c as a function of n occurs when the chemical potential is in the range $\tilde{\mu}_{\min} < \tilde{\mu} < 0$. We now specialize to the 2D case, where $\tilde{\mu}_{\min} = -\exp(-2/\tilde{\lambda}_{11})$; the 3D case is similar. Substituting $\tilde{\mu} = -\exp(-2/\tilde{\lambda}_{11})$ in the density equation (9b), we get a relation between \tilde{n} and \tilde{T}_c , which is accurate near the band minimum:

$$\tilde{n} = \tilde{T}_c \left[\frac{m_1}{m} \ln \left(1 + e^{\frac{-\exp(-2/\tilde{\lambda}_{11})}{\tilde{T}_c}} \right) + \frac{m_2}{m} \ln \left(1 + e^{\frac{-\exp(-2/\tilde{\lambda}_{11}) - \tilde{E}_{02}}{\tilde{T}_c}} \right) \right]. \quad (23)$$

This relation correctly predicts the near-band edge behavior as shown in Fig. 7(a) and in particular gives the linear dependence $\tilde{n} = \tilde{T}_c (m_2/m) \ln(2)$ at the transition point where $\tilde{E}_{02} = \tilde{\mu}_{\min}$. In 3D the corresponding formula for $\tilde{E}_{02} = \tilde{\mu}_{\min}$ is $\tilde{n} = \tilde{T}_c^{3/2} (m_2/m)^{3/2} |\text{Li}_{3/2}(-1)|$. It is remarkable that, at the transition point, the critical temperature is entirely controlled by the properties of the non-superconducting band. For $\tilde{\lambda}_{11} < 1$ in 3D we have $\tilde{\mu}_{\min} = 0$ and the NB does not change the analytic structure of the $T_c(n)$ curve.

If $\tilde{E}_{02} < \tilde{\mu}_{\min}$, the SB is not populated at low density and superconductivity appears in 2D for densities larger than $\tilde{n}_0 = (m_2/m)(\tilde{\mu}_{\min} - \tilde{E}_{02})$ and in 3D for densities larger than $\tilde{n}_0 = 4/(3\sqrt{\pi})(m_2/m)^{3/2}(\tilde{\mu}_{\min} - \tilde{E}_{02})^{3/2}$. In all cases, the $T_c(n)$ curve is “stretched” to higher densities with respect to the one-band result (see Fig. 7) due to the carriers “lost” in the NB. For instance, if the band minima are degenerate, we see from Eqs. (9) that the one-band $T_c(n)$ curve is simply modified by a rescaling of the density $n \rightarrow n/[1 + (m_1/m_2)^{d/2}]$. This implies that the critical temperature is necessarily reduced by a non-superconducting band, in the absence of inter-band coupling.

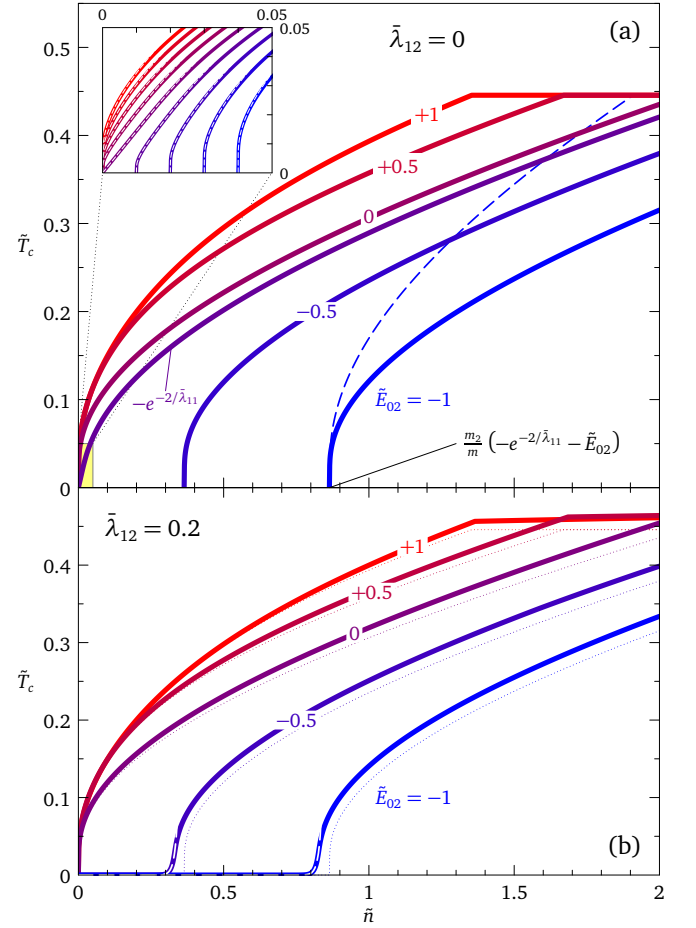


FIG. 7. BCS critical temperature for two parabolic bands in two dimensions, with coupling constants $\tilde{\lambda}_{11} = 1$, $\tilde{\lambda}_{22} = 0$, and (a) $\tilde{\lambda}_{12} = 0$, (b) $\tilde{\lambda}_{12} = 0.2$. E_{02} is the energy minimum of the second band, measured from the energy minimum of the first. The masses are $m_1 = m_2 = m$. The dashed line in (a) is the one-band result, shifted horizontally for easier comparison. (Inset) Blowup of the transition region. Curves are shown for $\tilde{E}_{02} = -\exp(-2/\tilde{\lambda}_{11}) + \delta\tilde{E}$, with $\delta\tilde{E}$ ranging from -0.04 (blue, right) to $+0.04$ (red, left). Note the linear behavior for $\delta\tilde{E} = 0$. The white dashed lines show Eq. (23). In (b), the dotted lines are the result for $\tilde{\lambda}_{12} = 0$ and the dashed white lines show Eq. (24).

Both attractive and repulsive inter-band interactions increase T_c for two bands,^{22,23} as illustrated by the fact that Eqs. (9) involve only $\tilde{\lambda}_{12}^2$: inter-band interactions do not induce inter-band pairing in the present model, but reinforce the intra-band pairing by second-order processes involving the other band. If T_c starts at finite density, the inter-band coupling leads to a tail in the $T_c(n)$ curve for $\tilde{n} < \tilde{n}_0$. In the regime where the chemical potential is below the SB, but well into the NB, the ψ_d functions of the SB and NB can be replaced by Eq. (10) and by Eq. (12) or (13), respectively, and the asymptotic expression of T_c can be deduced. In 2D, for instance, we find:

$$\tilde{T}_c = \frac{2e^\gamma}{\pi} \sqrt{\tilde{n} \frac{m}{m_2}} \exp \left\{ \frac{1}{\tilde{\lambda}_{12}^2} \left[\tilde{\lambda}_{11} + \frac{2}{\ln(-\tilde{E}_{02} - \tilde{n} \frac{m}{m_2})} \right] \right\}. \quad (24)$$

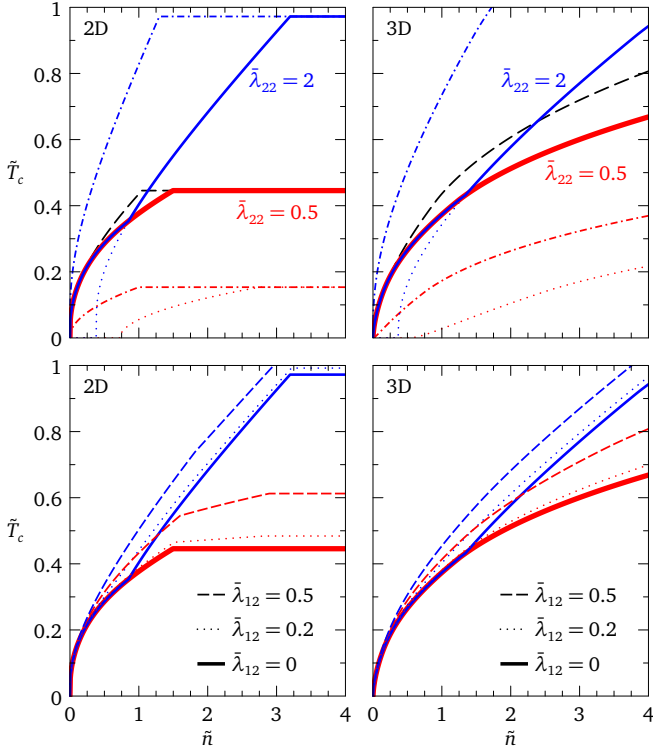


FIG. 8. Top panels: change of T_c induced by a second superconducting band in 2D and 3D, without inter-band coupling. Dashed black lines: critical temperature for a single band with coupling $\tilde{\lambda}_{11} = 1$ and mass $m_1/m = 1$. Solid lines: critical temperature for the two-band system with $\tilde{E}_{02} - \tilde{E}_{01} = 0.75$, $m_2 = m_1$, and coupling $\tilde{\lambda}_{22} = 0.5$ (red) and $\tilde{\lambda}_{22} = 2$ (blue). Dash-dotted: case of the second band alone. Dotted: case of the two-band system with $\tilde{\lambda}_{11} = 0$. Bottom panels: increase of T_c by inter-band coupling. Solid lines: no inter-band coupling, same data and coloring as in the top panels. Dotted and dashed lines correspond to inter-band coupling $\tilde{\lambda}_{12} = 0.2$ and 0.5 , respectively.

This is compared with the numerical result in Fig. 7(b). If $\tilde{n}_0 = 0$, on the other hand, the inter-band coupling has only a marginal effect on T_c , because the latter is controlled near the band edge by the proximity of μ to the bottom of the superconducting band.

We move on to the case of two superconducting bands and begin with general trends. The observation that T_c is an increasing function of density²⁴ remains true in the near-band edge regime. It is possible to show that the property $dT_c/dn \geq 0$ is guaranteed by Eqs. (9) for an arbitrary number of bands and any values of the coupling constants. It is a consequence of the facts that $d\mu/dn > 0$, $\partial_a \psi_d(a, b) > 0$, and $\partial_b \psi_d(a, b) < 0$. Reference 6 reports a nonmonotonic dependence of the critical temperature on carrier concentration in doped SrTiO₃: this can not be interpreted on the basis of Eqs. (9), without invoking density-dependent interactions.

A second band can nevertheless lead to a decrease of T_c at fixed density. Specifically, consider a one-band system at some density with coupling $\tilde{\lambda}_{11}$ and critical temperature T_c^0 ;

add a second band at higher energy with coupling $\tilde{\lambda}_{22} \leq \tilde{\lambda}_{11}$ and no inter-band coupling; then the two-band system with the same density has $T_c \leq T_c^0$, the equal sign being possible only in 2D at sufficiently high density. This can be proven as follows. Let μ^0 be the chemical potential for a single band. The gap equation in this case is $1 - \tilde{\lambda}_{11}\psi_1^0 = 0$, with $\psi_1^0 \equiv \psi_d(1 + \tilde{\mu}^0, \tilde{T}_c^0)$. For the two-band problem, take $E_{01} = 0$, $E_{02} > 0$ and define $\psi_1 \equiv \psi_d(1 + \tilde{\mu}, \tilde{T}_c)$, $\psi_2 \equiv \psi_d(1 + \tilde{\mu} - \tilde{E}_{02}, \tilde{T}_c)$. The gap equation is $1 - \tilde{\lambda}_{11}\psi_1 = \tilde{\lambda}_{22}\psi_2 - \tilde{\lambda}_{11}\tilde{\lambda}_{22}\psi_1\psi_2$. Both gap equations being verified with the same density, we have $\mu < \mu^0$. Writing $\psi_1 = \psi_1^0 + \delta\psi_1$, we see that the second gap equation has two solutions, which are $\delta\psi_1 = 0$ and $\psi_2 = 1/\tilde{\lambda}_{22}$. The solution $\delta\psi_1 = 0$, together with $\mu < \mu^0$, clearly implies $T_c \leq T_c^0$, the equal sign being possible only in 2D when $\tilde{\mu} > 1$ (see Fig. 2). Together with $\tilde{\lambda}_{22} \leq \tilde{\lambda}_{11}$, the second solution implies $\psi_d(1 + \tilde{\mu} - \tilde{E}_{02}, \tilde{T}_c) \geq \psi_d(1 + \tilde{\mu}^0, \tilde{T}_c^0)$, which again requires $T_c \leq T_c^0$.

If the second band has a coupling $\tilde{\lambda}_{22} > \tilde{\lambda}_{11}$, T_c exceeds T_c^0 at high enough density and follows the dependence that would correspond to a non-superconducting first band. In 2D T_c saturates to the value associated with the strongest band, in the regime where the chemical potential recovers its noninteracting value, while in 3D T_c remains below the value associated with the strongest band, due to a lower chemical potential. These various trends are illustrated in Fig. 8 (top panels). Figure 8 (bottom panels) shows the effect of inter-band interaction, which is generically an increase of T_c .

V. CONCLUSION

In summary, in the low-density regime where the dynamical range of the pairing interaction is set by the band edge, the BCS critical temperature T_c depends on the electron density n in a nonanalytic way. For parabolic bands, we provided exact asymptotic formula describing this dependency, taking into account the energy variation of the electronic DOS, as well as the variation of the chemical potential with interaction strength and temperature. In one and two dimensions and in three dimensions at strong enough coupling, the chemical potential (at T_c) becomes negative at low density and as a result the $T_c(n)$ curve starts with infinite slope and increases faster than any power of n . A negative chemical potential results in one and two dimensions because of the DOS discontinuity, such that the spreading of the momentum distribution by the pairing interaction, no matter how small, suffices to produce a finite density; in three dimensions where the DOS vanishes at the band edge, a finite coupling is needed to have a negative chemical potential. Otherwise, i.e., in three dimensions at weak coupling, the chemical potential approaches zero at low density, the $T_c(n)$ curve starts with zero slope, and it increases slower than any power of n .

Our results are relevant for low-density superconductors that are not in the BEC regime. In SrTiO₃, oxygen reduction and niobium doping allows one to tune the carrier density⁶ in a range such that the dimensionless density \tilde{n} varies typi-

cally between 10^{-2} and 10. In the $\text{LaAlO}_3/\text{SrTiO}_3$ interface, the gate-tuned sheet carrier density can also be tuned²⁵ such that \tilde{n} varies typically from 10^{-1} to 1. In the low-density range of these domains, our exact formula differ from the usual formulae valid at higher densities. In the numerical illustrations of the present paper, we have used coupling constants $\tilde{\lambda}$ of order one, which may appear very large in comparison to the typical values of the order 0.1 reported for SrTiO_3 . We emphasize, however, that our definition of the coupling constants differs from the usual definition, such that in three dimensions ours are bigger than the usual ones by a factor $(\mu/\hbar\omega_D)^{1/2}$, which is typically three in SrTiO_3 .

The observation that T_c is a nonanalytic function of n near a band bottom calls for a reconsideration of the problem of shape resonances. These are oscillations of T_c in a quasi-two dimensional superconductor confined in a slab, as a function of the slab thickness. The oscillations arise when the chemical potential crosses the bottom of one of the confinement-induced subbands and were presented in the literature on the subject as discontinuities.⁴ Our results show that such discontinuities are artifacts, because T_c vanishes continuously at a band edge in any dimension. The actual dependence of T_c on the slab thickness is therefore a continuous function, which remains to be investigated. A particularly interesting system in this respect is the $\text{LaAlO}_3/\text{SrTiO}_3$ interface, which cumulates the characteristics of being a low-density superconducting system, confined in a quasi-two dimensional geometry, and also a multi-band system.

ACKNOWLEDGMENTS

We acknowledge fruitful discussions with J.-M. Triscone, S. Gariglio, and M. Grilli. This work was supported by the Swiss National Science Foundation under Division II.

Appendix A: Simple proof of Eq. (4)

The density of a free-electron gas in dimension d is proportional to the volume of the d -dimensional Fermi sphere, smeared by the Fermi function:

$$\begin{aligned} n &= 2 \int \frac{d^d k}{(2\pi)^d} \frac{1}{\exp\left(\frac{\hbar^2 k^2/2m - \mu}{k_B T}\right) + 1} \\ &= 2 \int \frac{d^d k}{(2\pi)^d} \frac{x}{x - \exp\left(\frac{\hbar^2 k^2}{2mk_B T}\right)}, \end{aligned}$$

with $x = -\exp(\mu/k_B T)$. In order to evaluate the integral, we use the expansion $x/(x - a) = -\sum_{q=1}^{\infty} x^q/a^q$ and we write $k^2 = \sum_{i=1}^d k_i^2$. This leads to a product of gaussian

integrals:

$$\begin{aligned} n &= -2 \sum_{q=1}^{\infty} x^q \prod_{i=1}^d \int_{-\infty}^{\infty} \frac{dk_i}{2\pi} \exp\left(-q \frac{\hbar^2 k_i^2}{2mk_B T}\right) \\ &= -2 \sum_{q=1}^{\infty} x^q \prod_{i=1}^d \sqrt{\frac{mk_B T}{2\pi\hbar^2 q}} = -2 \left(\frac{mk_B T}{2\pi\hbar^2}\right)^{\frac{d}{2}} \sum_{q=1}^{\infty} \frac{x^q}{q^{d/2}}. \end{aligned}$$

Considering the Taylor expansion of the polylogarithm, we see that the q -sum in the last expression is $\text{Li}_{d/2}(x)$, which proves Eq. (4).

Appendix B: Results for one parabolic band in 1D

With the proviso that the factor $(d-1)\pi$ in Eqs. (3) and (7) be replaced by 1, the equations (2) to (9) are valid for $d=1$. The asymptotic properties of the function $\psi_1(a, b)$ are

$$\begin{aligned} \psi_1(0 < a < 1, b \rightarrow 0) &= \frac{\sin^{-1}(\sqrt{a})}{\sqrt{1-a}} \approx \frac{\pi/2}{\sqrt{1-a}} - 1 \\ \psi_1(1 < a < 2, b \rightarrow 0) &= \frac{1}{\sqrt{a-1}} \ln \left(\frac{a-1}{\sqrt{a} + \sqrt{a-1}} \frac{8e^\gamma}{\pi b} \right) \\ \psi_1(a > 2, b \rightarrow 0) &= \frac{1}{\sqrt{a-1}} \\ &\quad \times \ln \left(\frac{a-1}{(\sqrt{a} + \sqrt{a-1})(\sqrt{a-1} + \sqrt{a-2})} \frac{8e^\gamma}{\pi b} \right). \end{aligned}$$

The corresponding weak-coupling approximations in the regime $\tilde{n} \gtrsim 1$ are

$$\begin{aligned} \tilde{T}_c &\approx \frac{8e^\gamma}{\pi} \exp\left(-\frac{1}{\tilde{\lambda}/\sqrt{\tilde{\mu}}}\right) \frac{1}{1 + \sqrt{1+1/\tilde{\mu}}} \\ &\quad \times \begin{cases} \sqrt{\tilde{\mu}} & \tilde{\mu} \lesssim 1 \\ \frac{1}{1 + \sqrt{1-1/\tilde{\mu}}} & \tilde{\mu} > 1 \end{cases} \quad (d=1), \quad (\text{B1}) \end{aligned}$$

in agreement with the result of Ref. 2, where $\tilde{\lambda}/\sqrt{\tilde{\mu}}$ is the coupling constant evaluated at the chemical potential. In the low-density limit, like in 2D, the chemical potential approaches a finite negative value for all couplings, given by the solution of $1/\tilde{\lambda} = \sin^{-1}(\sqrt{1+\tilde{\mu}_{\min}})/\sqrt{-\tilde{\mu}_{\min}} \approx (\pi/2)/\sqrt{-\tilde{\mu}_{\min}} - 1$. We can use the expansion $-\text{Li}_{1/2}(-e^x) \rightarrow e^x$ for large negative x and deduce the relation $\tilde{\mu} = \tilde{T}_c \ln(\tilde{n}/\tilde{T}_c^{1/2})$. We find for \tilde{T}_c

$$\tilde{T}_c = \tilde{n}^2 \exp \left[W \left(\frac{1}{2} \left(\frac{\pi\tilde{\lambda}}{1+\tilde{\lambda}} \right)^2 \frac{1}{\tilde{n}^2} \right) \right] \quad (d=1, n \rightarrow 0). \quad (\text{B2})$$

The numerical results are shown in Fig. 9 and compared with the analytical formula (B1) and (B2). Eq. (B1) works well at high density, but severely breaks down at low density, even at weak coupling. The cancellation of errors observed

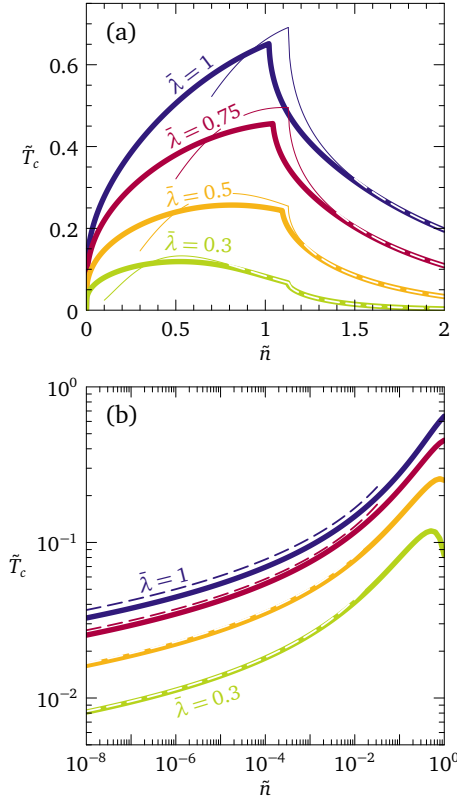


FIG. 9. (a) BCS critical temperature as a function of electron density for one parabolic band in one dimension. T_c is expressed in units of $\hbar\omega_D/k_B$ and n in units of $2[m\omega_D/(2\pi\hbar)]^{1/2}$. The thin and dashed lines show Eq. (B1), evaluated using $\tilde{\mu}_0 = (\pi/4)\tilde{n}^2$ for $\tilde{\mu}$. (b) Same data on a log-log scale. The dashed lines show Eq. (B2).

in the 3D case also occurs here to some extent, but the main issue is that Eq. (B1) fails to describe the regime where $\tilde{\mu} < 0$ at low density, while in 3D this regime is absent for $\tilde{\lambda} < 1$. Eq. (B2) is accurate at weak coupling where $-\tilde{\mu} \ll 1$ and has the small inaccuracy associated with the approximation made in solving for $\tilde{\mu}$ at larger coupling.

Appendix C: Gap to T_c ratio in the low-density limit

We give here the zero-temperature gap explicitly for one band in 2D, as a function of density and coupling. This can be combined with the result (19) in order to obtain the exact gap to T_c ratio in the low-density limit. The expression of the density at $T = 0$ is

$$n = \int_{-\infty}^{\infty} d\xi N_0(\mu + \xi) \left(1 - \frac{\xi}{\sqrt{\xi^2 + \Delta_\xi^2}} \right), \quad (C1)$$

where $N_0(E)$ is the normal-state DOS given by Eq. (3) and $\Delta_\xi = \theta(\hbar\omega_D - |\xi|)\Delta$ with Δ the zero-temperature gap. We set $E_{0\alpha} = 0$ and $m = m_\alpha$ as in Sec. III and move to dimensionless variables. In 2D we have at $T = 0$:

$$\tilde{n} = \begin{cases} 0 & \tilde{\mu} < -1 \\ \frac{1}{2} \left(\tilde{\mu} + 1 + \sqrt{\tilde{\mu}^2 + \tilde{\Delta}^2} - \sqrt{1 + \tilde{\Delta}^2} \right) & -1 < \tilde{\mu} < 1 \\ \tilde{\mu} & \tilde{\mu} > 1. \end{cases} \quad (C2)$$

The gap equation is obtained by replacing $\tanh(\dots)$ by unity in Eq. (1a). For one band in 2D we find

$$1/\tilde{\lambda} = \begin{cases} 0 & \tilde{\mu} < -1 \\ \frac{1}{2} \ln \left(\frac{1 + \sqrt{1 + \tilde{\Delta}^2}}{\sqrt{\tilde{\mu}^2 + \tilde{\Delta}^2} - \tilde{\mu}} \right) & -1 < \tilde{\mu} < 1 \\ \ln \left(\frac{1 + \sqrt{1 + \tilde{\Delta}^2}}{\tilde{\Delta}} \right) & \tilde{\mu} > 1. \end{cases} \quad (C3)$$

For $\tilde{\mu} > 1$, the gap is density-independent and given by $\tilde{\Delta} = 1/\sinh(1/\tilde{\lambda})$; combined with the weak-coupling result (17), this yields the usual weak-coupling BCS ratio $\Delta/(k_B T_c) = \pi/e^\gamma$. In the low-density regime $\tilde{\mu} < 1$, we eliminate $\tilde{\Delta}$ among Eqs. (C2) and (C3) to find $\tilde{\mu} = \tilde{n} + (\tilde{n} - 1)e^{-2/\tilde{\lambda}}$. Solving for the gap, we then arrive at:

$$\tilde{\Delta} = \frac{\sqrt{\tilde{n} + \tilde{n}(\tilde{n} - 1)e^{-2/\tilde{\lambda}}}}{\sinh(1/\tilde{\lambda})} \quad (\tilde{n} < 1). \quad (C4)$$

Comparing Eqs. (C4) and (19), we see that T_c increases faster than Δ with increasing density. As a result the gap to T_c ratio vanishes for $n \rightarrow 0$, as we show in Fig. 10.

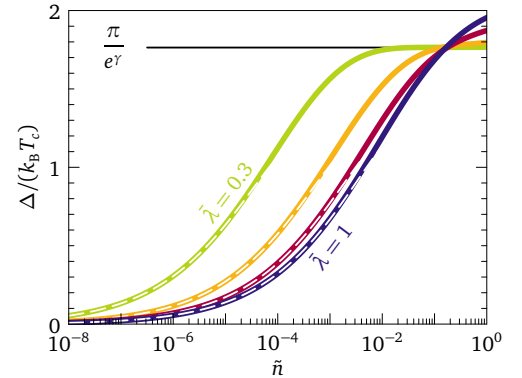


FIG. 10. Zero-temperature gap (Δ) to T_c ratio calculated numerically for one parabolic band in two dimensions. Curves are drawn as a function of density n expressed in units of $m\omega_D/(\pi\hbar)$ for $\tilde{\lambda} = 0.3, 0.5, 0.75$, and 1 . The dashed lines show the ratio of Eqs. (C4) and (19). The horizontal line indicates the BCS weak-coupling ratio $\pi/e^\gamma \approx 1.76$.

* To whom correspondence should be addressed. E-mail: christophe.berthod@unige.ch

¹ J. Bardeen, L. N. Cooper, and J. R. Schrieffer, *Microscopic theory of superconductivity*, *Phys. Rev.* **108**, 1175 (1957).

- ² D. M. Eagles, *Predicted Transition Temperatures of Very Thin Films and Whiskers of Superconducting Semiconductors—Application to SrTiO₃*, *Phys. Rev.* **164**, 489 (1967).
- ³ C. J. Thompson and J. M. Blatt, *Shape resonances in superconductors - II simplified theory*, *Phys. Lett.* **5**, 6 (1963).
- ⁴ See, e.g., A. Romero-Bermúdez and A. M. García-García, *Shape resonances and shell effects in thin-film multiband superconductors*, *Phys. Rev. B* **89**, 024510 (2014), and references therein.
- ⁵ D. M. Eagles, *Effective Masses in Zr-Doped Superconducting Ceramic SrTiO₃*, *Phys. Rev.* **178**, 668 (1969); *Possible Pairing without Superconductivity at Low Carrier Concentrations in Bulk and Thin-Film Superconducting Semiconductors*, *Phys. Rev.* **186**, 456 (1969).
- ⁶ X. Lin, G. Bridoux, A. Gourgout, G. Seyfarth, S. Krämer, M. Nardone, B. Fauqué, and K. Behnia, *Critical Doping for the Onset of a Two-Band Superconducting Ground State in SrTiO_{3-δ}*, *Phys. Rev. Lett.* **112**, 207002 (2014).
- ⁷ M. Ahrens, R. Merkle, B. Rahmati, and J. Maier, *Effective masses of electrons in n-type SrTiO₃ determined from low-temperature specific heat capacities*, *Physica B: Cond. Mat.* **393**, 239 (2007).
- ⁸ P. Zubko, S. Gariglio, M. Gabay, P. Ghosez, and J.-M. Triscone, *Interface Physics in Complex Oxide Heterostructures*, *Ann. Rev. Cond. Mat. Phys.* **2**, 141 (2011).
- ⁹ R. Pentcheva and W. E. Pickett, *Electronic phenomena at complex oxide interfaces: insights from first principles*, *J. Phys. Condens. Matter* **22**, 043001 (2010).
- ¹⁰ C. Cancellieri, M. L. Reinle-Schmitt, M. Kobayashi, V. N. Strocov, P. R. Willmott, D. Fontaine, P. Ghosez, A. Filippetti, P. Delugas, and V. Fiorentini, *Doping-dependent band structure of LaAlO₃/SrTiO₃ interfaces by soft x-ray polarization-controlled resonant angle-resolved photoemission*, *Phys. Rev. B* **89**, 121412 (2014).
- ¹¹ V. L. Berezinskii, *Destruction of Long-range Order in One-dimensional and Two-dimensional Systems having a Continuous Symmetry Group I. Classical Systems*, *Zh. Eksp. Teor. Fiz.* **59**, 907 (1970) [*Sov. Phys. JETP* **32**, 493 (1971)].
- ¹² J. M. Kosterlitz and D. J. Thouless, *Ordering, metastability and phase transitions in two-dimensional systems*, *J. Phys. C: Solid State Phys.* **6**, 1181 (1973).
- ¹³ P. Nozières and S. Schmitt-Rink, *Bose Condensation in an Attractive Fermion Gas: From Weak to Strong Coupling Superconductivity*, *J. Low. Temp. Phys.* **59**, 195 (1985).
- ¹⁴ For a recent review, see M. Randeria and E. Taylor, *Crossover from Bardeen-Cooper-Schrieffer to Bose-Einstein Condensation and the Unitary Fermi Gas*, *Ann. Rev. Cond. Mat. Phys.* **5**, 209 (2014).
- ¹⁵ D. Innocenti, N. Poccia, A. Ricci, A. Valletta, S. Caprara, A. Perali, and A. Bianconi, *Resonant and crossover phenomena in a multiband superconductor: Tuning the chemical potential near a band edge*, *Phys. Rev. B* **82**, 184528 (2010); D. Innocenti, S. Caprara, N. Poccia, A. Ricci, A. Valletta, and A. Bianconi, *Shape resonance for the anisotropic superconducting gaps near a Lifshitz transition: the effect of electron hopping between layers*, *Supercond. Sci. Technol.* **24**, 015012 (2011); A. Guidini and A. Perali, *Band-edge BCS-BEC crossover in a two-band superconductor: physical properties and detection parameters*, *Supercond. Sci. Technol.* **27**, 124002 (2014).
- ¹⁶ C. Hainzl and R. Seiringer, *Critical temperature and energy gap for the BCS equation*, *Phys. Rev. B* **77**, 184517 (2008).
- ¹⁷ D. van der Marel, *Anomalous behaviour of the chemical potential in superconductors with a low density of charge carriers*, *Physica C* **165**, 35 (1990).
- ¹⁸ The standard numerical integration packages will generally fail to produce an accurate result for Eq. (6), or they will take a prohibitively long time to converge, especially in the limit $b \rightarrow 0$ of interest to us. For a fast and accurate numerical evaluation of Eq. (6), we have used the representation of the Fermi function proposed in Ref. 19. With fourteen Osaki poles and residues, we build a representation of the function $\tanh(x/2)$ which has an accuracy of $\sim 10^{-16}$ for all x , setting the function to ± 1 for $|x| > 16\ln(10)$. With this representation, Eq. (6) can be evaluated analytically. This provides a very fast implementation of the functions $\psi_d(a, b)$, with a machine-precision accuracy of $\sim 10^{-16}$.
- ¹⁹ T. Ozaki, *Continued fraction representation of the Fermi-Dirac function for large-scale electronic structure calculations*, *Phys. Rev. B* **75**, 035123 (2007).
- ²⁰ A. Perali, A. Bianconi, A. Lanzara, and N. L. Saini, *The gap amplification at a shape resonance in a superlattice of quantum stripes: A mechanism for high T_c*, *Solid State Comm.* **100**, 181 (1996).
- ²¹ For a recent review, see: M. Zehetmayer, *A review of two-band superconductivity: materials and effects on the thermodynamic and reversible mixed-state properties*, *Supercond. Sci. Tech.* **26**, 043001 (2013).
- ²² H. Suhl, B. T. Matthias, and L. R. Walker, *Bardeen-Cooper-Schrieffer Theory of Superconductivity in the Case of Overlapping Bands*, *Phys. Rev. Lett.* **3**, 552 (1959).
- ²³ A. Bussmann-Holder, R. Micnas, and A. R. Bishop, *Enhancements of the superconducting transition temperature within the two-band model*, *Eur. Phys. J. B* **37**, 345 (2004).
- ²⁴ R. M. Fernandes, J. T. Haraldsen, P. Wölfle, and A. V. Balatsky, *Two-band superconductivity in doped SrTiO₃ films and interfaces*, *Phys. Rev. B* **87**, 014510 (2013).
- ²⁵ A. D. Caviglia, S. Gariglio, N. Reyren, D. Jaccard, T. Schneider, M. Gabay, S. Thiel, G. Hammerl, J. Mannhart, and J.-M. Triscone, *Electric field control of the LaAlO₃/SrTiO₃ interface ground state*, *Nature* **456**, 624 (2008).